THESIS FOR THE DEGREE OF MASTER OF SCIENCE

Unsteady-RANS Simulation of Turbulent Trailing-Edge Flow

VAGESH D.NARASIMHAMURTHY

Department of Thermo and Fluid Dynamics

CHALMERS UNIVERSITY OF TECHNOLOGY

Göteborg, Sweden, 2004

Unsteady-RANS Simulation of Turbulent Trailing-Edge Flow
VAGESH D.NARASIMHAMURTHY

Diploma Work 04/31

Institutionen för termo- och fluiddynamik
Chalmers Tekniska Högskola
SE-412 96 Göteborg, Sweden
Phone +46-(0)31-7721400
Fax: +46-(0)31-180976

Printed at Chalmers Reproservice
Göteborg, Sweden 2004

Unsteady-RANS Simulation of Turbulent Trailing-Edge Flow

by

Vagesh D.Narasimhamurthy
vagesh@student.chalmers.se

Abstract

Unsteady RANS (Reynolds Averaged Navier Stokes) computations of turbulent trailing-edge flow have been carried out at a Reynolds number of 1000 (based on the free-stream quantities and the trailing-edge thickness) using a 3D Finite Volume code, in which a Low Reynolds Number (LRN) $k-\varepsilon$ model and $\overline{v^2}-f$ model were implemented. The realizability constraints suggested by Durbin was also implemented in the models to study their effect on the unsteady vortex shedding. Central differencing scheme was used for all the computations, but van-Leer scheme was also tried in order to study the influence of numerical schemes on unsteady vortex shedding.

Results from a Direct Numerical Simulation (DNS) of the same flow are available for comparison and assessment of turbulence models used in the URANS code. Two-dimensional URANS calculations are carried out with turbulence mean properties from the DNS used at the inlet; the inflow boundary-layer thickness is 6.42 times the trailing-edge thickness, close to typical turbine blade flow applications.

The LRN $k-\varepsilon$ model failed to capture unsteady vortex shedding, but when realizability constraint was implemented, the model captures flow unsteadiness. Many of the key flow features observed in DNS are also predicted by the modelling; the flow oscillates in a similar way to that found in bluff-body flow with a von Kármán vortex sheet produced downstream. The recirculation bubble predicted by unsteady RANS has a similar shape and a length close to DNS. It was found that the unsteadiness plays an important role in the near wake, comparable to the modelled turbulence. A spectral analysis applied to the lift and pressure drag coefficients show that a Strouhal number based on the trailing-edge thickness is 0.104, very close to DNS value. It was found that van-Leer scheme being a bounded scheme and dissipative in nature, produces higher resolved kinetic energy compared to central difference scheme; the reason for which has to be investigated.

Acknowledgments

I would like to convey my deepest regards to my supervisor, Prof. Lars Davidson for all his support, motivation and guidance. He has been a constant source of encouragement for me through out this work, especially during those times when i felt things are moving at snails pace.

I would like to thank Andreas Sveningsson for spending a large part of his valuable time on my desk, helping me from CALC to LaTeX. Without his help the thesis wouldn't have been into this shape. Thanks Andreas.

I would also like to thank Dr. Yufeng Yao, at School of Engineering, Kingston University, for providing the DNS data.

Finally, I would like to thank everyone at the department, especially Walter Gyllenram and Niklas Andersson for their help.

Nomenclature

Upper-case Roman

A	Area
C	Center line
C_L	Lift co-efficient
C_D	Pressure drag co-efficient
$C_{L'}$	RMS lift co-efficient
$C_{D'}$	RMS pressure drag co-efficient
L	Length
Pr	Prandtl number
P_k	Production term
Re_h	Reynolds number based on the trailing-edge thickness
S_{ij}	Strain rate tensor
St	Strouhal number ($St = (f_s h)/U_e$)
SU	Source term
SP	Sink term

Lower-case Roman

f_s	shedding frequency
h	trailing-edge thickness
k	turbulent kinetic energy
k_{mod}	modelled kinetic energy
k_{res}	resolved kinetic energy
p	pressure
pp	pressure correction
t	time
u_i	cartesian components of velocity vector
u	streamwise velocity component
v	cross-streamwise velocity component
w	spanwise velocity component
u^*	wall friction velocity, $u^* = \sqrt{\tau_w/\rho}$
x_i	cartesian coordinate vector component
y^+	dimensionless wall normal distance

Upper-case Greek

Φ	Dependent variables
Δt	Time step
$\Delta x, \Delta y$	Grid spacing along x and y respectively

Lower-case Greek

δ_{ij}	Kronecker delta
ε	Dissipation
μ	Dynamic viscosity
ν	kinematic viscosity, $\nu = \mu/\rho$
ν_t	Turbulent or eddy viscosity
τ_w	Wall shear stress
ρ	density
σ_{ij}	viscous stress tensor
$\sigma_k, \sigma_\varepsilon$	Turbulent Prandtl numbers

Subscripts

n, s, e, w	north, south, east and west respectively
∞	free stream or ambient conditions
$b\,l$	boundary layer

Superscripts

$\prime$	Modelled turbulent fluctuation
$\prime\prime$	Resolved fluctuation
$\sim$	Instantaneous component

Symbols

$\overline{(\dots)}$	Ensemble averaged quantity
$\langle \dots \rangle$	time averaged quantity

Abbreviations

CFD	Computational Fluid Dynamics
CFL	Courant-Friedrichs-Lewy
DNS	Direct Numerical Simulation
FVM	Finite Volume Method
LRN	Low Reynolds Number
LES	Large Eddy Simulation
PDE	Partial Differential Equation
TDMA	Tri-Diagonal MAtrix Algorithm
URANS	Unsteady Reynolds Averaged Navier-Stokes

Contents

Abstract **iii**

Acknowledgments **v**

Nomenclature **vii**

1 Introduction **1**
1.1 What is a trailing-edge flow? 1
1.2 Scope of present work 1

2 Governing equations **3**
2.1 Instantaneous equations of motion 3
2.2 Averaged equations of motion-(U)RANS 4
2.3 Eddy viscosity models 5
2.3.1 Abe-Kondoh-Nagano k-ε model 6
2.3.2 Realizability and production (P_k) limiter 7
2.3.3 Realizable $\overline{v^2} - f$ model 7

3 Numerical method and the flow domain **11**
3.1 The solver CALC-BFC 11
3.2 The flow domain 11
3.3 The grid 11
3.4 Numerical schemes 13
3.5 Boundary conditions 13
3.6 The TDMA solver 13

4 Implementation of blockage **15**
4.1 Implementation 15
4.2 Validation 18

5 Results and discussion **21**
5.1 Grid refinement study 21
5.2 Vortex shedding 21
5.3 Velocity profiles and streamlines 24
5.4 Resolved and modelled quantities 24
5.4.1 Resolved and modelled turbulent kinetic energy . . 24

5.4.2 Dissipation 27
5.4.3 Resolved and modelled stresses 31
5.5 Influence of discretizing scheme 31

6 Conclusions **35**

7 Future Work **37**

Chapter 1

Introduction

1.1 What is a trailing-edge flow?

A simple 2D configuration of a trailing-edge flow is shown in Figure 1.1. The turbulent flow over the trailing-edge presents difficulties for numerical simulation because of the sudden removal of the solid wall and consequent turbulence interactions. The flow characteristics change from boundary-layer (i.e. wall-bounded shear-layer) upstream to wake flow (i.e. free shear-layer) down-stream. Complicated flow phenomena occur in the near-wake, largely due to the flow separation and instability. The flow oscillates downstream in the wake in a similar way to that observed in bluff-body flow, with a von Kármán vortex sheet produced. This flow also shows complicated turbulence kinetic energy transport, notably the balance between the energy production and dissipation in the upstream boundary-layer is destroyed and then re-created in the wake downstream, where a new equilibrium state is reached.

Obviously this flow has many practical engineering applications, for example drag reduction and noise emission in aeronautical and turbo machinery industries, turbine rotor blade design and airframe design applications.

1.2 Scope of present work

Yao et al.[12] have previously carried out a Direct Numerical Simulation (DNS) for this type of flow with a Reynolds number of 1000, based on the free-stream quantities and the trailing edge thickness (h), and with the incoming turbulent boundary-layer displacement thickness δ^* approximately equal to h.

Based on the success of DNS, Yao et al.[11] have also carried out 2D unsteady RANS (URANS) calculations, by applying the turbulence mean properties from DNS at the inlet and by using an unstructured com-

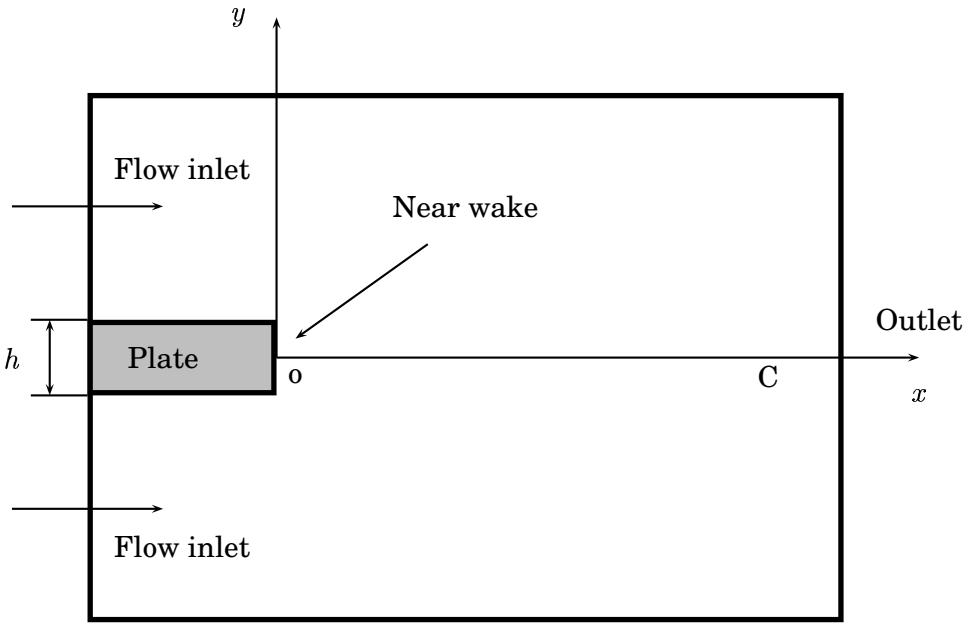

Figure 1.1: Rectangular trailing-edge plate configuration

pressible 3D code with two-equation ($k-\varepsilon$) turbulence model with Low Reynolds Number (LRN) near wall treatments. The inflow boundary-layer thickness was 6.42 times the trailing-edge thickness, close to typical turbine blade flow applications.

Their investigation revealed that their turbulence model under-predicts the reverse flow (the recirculation bubble predicted by their URANS had a length only half that of the DNS) and overpredicts the Strouhal number by a factor of two compared to DNS.

The present work considers 2D unsteady RANS (URANS) calculations of the same flow problem, in which a LRN $k-\varepsilon$ model and $\overline{v^2}-f$ models were implemented. The realizability constraints suggested by Durbin and production (P_k) limiters were used in the models to study their influence on unsteady vortex shedding. The URANS computations were carried out by applying the turbulence mean properties from DNS at the inlet and we have used an unstructured incompressible 3D finite-volume code. The problem is non-dimensionalized based on the trailing-edge thickness as the reference length and the free-stream velocity as the reference velocity.

Chapter 2

Governing equations

2.1 Instantaneous equations of motion

All fluid motions (where the continuum approximation is valid) are governed by a set of dynamical equations namely the *continuity equation* and the *momentum equation*,

$$\left[\frac{\partial \tilde{\rho}}{\partial t} + \tilde{u}_j \frac{\partial \tilde{\rho}}{\partial x_j}\right] + \tilde{\rho}\frac{\partial \tilde{u}_j}{\partial x_j} = 0 \tag{2.1}$$

$$\tilde{\rho}\left[\frac{\partial \tilde{u}_i}{\partial t} + \tilde{u}_j \frac{\partial \tilde{u}_i}{\partial x_j}\right] = -\frac{\partial \tilde{p}}{\partial x_i} + \frac{\partial \tilde{T}_{ij}^{(v)}}{\partial x_j} \tag{2.2}$$

where, $\tilde{u}_i = \tilde{u}_i(\vec{x}, t)$, a function of space $\vec{x}$ and time t. $\tilde{T}_{ij}^{(v)}(\vec{x}, t)$ is the viscous stress tensor.

The Newtonian closure for the viscous stress tensor relates it to the fluid motion using a property of fluid, molecular viscosity (μ).

$$\tilde{T}_{ij}^{(v)} = 2\mu\left(\tilde{s}_{ij} - \frac{1}{3}\tilde{s}_{kk}\delta_{ij}\right) \tag{2.3}$$

$\tilde{s}_{ij}$ is the instantaneous strain rate tensor given by,

$$\tilde{s}_{ij} = \frac{1}{2}\left(\frac{\partial \tilde{u}_i}{\partial x_j} + \frac{\partial \tilde{u}_j}{\partial x_i}\right) \tag{2.4}$$

For incompressible flows, the derivative of density following the fluid material is zero and hence 2.1 & 2.2 are simplified to,

$$\frac{\partial \tilde{u}_j}{\partial \tilde{x}_j} = 0 \tag{2.5}$$

$$\left[\frac{\partial \tilde{u}_i}{\partial t} + \tilde{u}_j \frac{\partial \tilde{u}_i}{\partial x_j}\right] = -\frac{1}{\rho}\frac{\partial \tilde{p}}{\partial x_i} + \nu\frac{\partial^2 \tilde{u}_i}{\partial x_j \partial x_j} \tag{2.6}$$

2.2 Averaged equations of motion-(U)RANS

Why average?

With the Newtonian closure for the viscous stress tensor we get a system of four equations involving four unknown variables. Assuming a complete set of boundary conditions being available the system of equations can be directly solved. This approach is called Direct Numerical Simulation (DNS). Performing DNS implies resolving all the scales. In turbulent flows the size of the turbulent flow structures cover a large spectrum ranging from the very small Kolmogorov scales to integral scales of the size of physical domain. This type of simulation is very expensive and beyond the scope of industrial applications. Also one should realize that in most applications the turbulence itself is of secondary interest, only its effect on the mean flow characteristics is important.

This means that it is convenient to analyze the turbulent flow in two parts, a mean (ensemble) component and a fluctuating component,

$$\begin{aligned} \tilde{u}_i &= \overline{U_i} + u_i' \\ \tilde{p} &= \overline{P} + p' \end{aligned} \tag{2.7}$$

This technique of decomposing is referred to as *Reynolds Decomposition*. Inserting these decomposed expressions in to the instantaneous equations and ensemble averaging results in *Reynolds Averaged Navier Stokes*(RANS) equations.

$$\frac{\partial \overline{U_j}}{\partial x_j} = 0 \tag{2.8}$$

$$\left[\frac{\partial \overline{U_i}}{\partial t} + \overline{U_j}\frac{\partial \overline{U_i}}{\partial x_j}\right] = -\frac{1}{\rho}\frac{\partial \overline{P}}{\partial x_i} + \nu\frac{\partial^2 \overline{U_i}}{\partial x_j \partial x_j} - \frac{\partial}{\partial x_j}\{\overline{u_i u_j}\} \tag{2.9}$$

Note that if the averages are defined as ensemble means, they are, in general, time-dependent, i.e. the dependent variables in 2.9 are not only a function of space, but also a function of time.

$$\overline{U}_i = \overline{U}_i(x_i, t),\ \overline{P} = \overline{P}(x_i, t) \text{ and } \overline{u_i u_j} = \overline{u_i u_j}(x_i, t) \tag{2.10}$$

The last term in 2.9 represents the correlation between fluctuating velocities and is called as *Reynolds stress tensor*. All the effects of turbulent fluid motion on the mean flow is lumped in to this single term by the process of averaging. This will enable great savings in terms of computational requirements. On the other hand, the process of averaging generated six new unknown variables. Now, in total we have ten unknowns (3-velocity, 1-pressure, 6-stresses) and only four equations (1-continuity, 3 components of Navier Stokes equation). This is referred

to as the *turbulence closure problem*. We will discuss in the next section how to solve this *closure problem*. But before that we have a question, what is URANS?

Some aspects of URANS

The URANS equations are the usual RANS equations as in 2.9. It is by convention we call it Unsteady-RANS since we retain the transient term $\partial\overline{U_i}/\partial t$ during computation. As we discussed earlier in 2.10 the averaged components are still a function of time. Therefore the results from the URANS are unsteady, but one is often interested only in the time-averaged flow. We denote here the time-averaged velocity as $\langle\overline{U}\rangle$, which means that we can decompose the results from URANS as a time-averaged part,$\langle\overline{U}\rangle$, a resolved fluctuation, u'', and the modelled turbulent fluctuation, u'. Therefore 2.7 becomes,

$$\tilde{u} = \overline{U} + u' = \langle\overline{U}\rangle + u'' + u' \tag{2.11}$$

2.3 Eddy viscosity models

In the previous section we came across the *turbulence closure problem*. In order to close the RANS equations, we can think of using the same idea behind the Newtonian closure for the viscous stress tensor. There, the viscous stress tensor is related to the fluid motion using a property of the fluid called molecular viscosity, μ.

A similar analogy which tries to relate the Reynolds stresses to the fluid motion through a new term called "eddy" or "turbulent" viscosity is referred to as *Boussinesq assumption*. According to which,

$$\rho\overline{u_i u_j} = -\mu_t\left(\frac{\partial\overline{U_i}}{\partial x_j} + \frac{\partial\overline{U_j}}{\partial x_i}\right) + \frac{2}{3}\rho\delta_{ij}k \tag{2.12}$$

This means that we represent the fluctuations with some kind of averaged quantity and try to find out how this quantity is coupled to the mean flow. The eddy viscosity is treated as a scalar quantity and is determined using a turbulent velocity scale $\mathcal{V}$ and a length scale l, based on the dimensional analysis.

$$\nu_t = \mathcal{V}l \tag{2.13}$$

There are different types of EVM's based on the way we close the eddy viscosity. Algebraic or zero equation EVM's normally use a geometric relation to compute the eddy viscosity. In one equation EVM's we solve for one turbulence quantity and a second turbulent quantity is obtained from algebraic expression. These two quantities are used to describe the eddy viscosity. In two equation EVM's, two turbulent quantities are solved to describe the eddy viscosity.

2.3.1 Abe-Kondoh-Nagano k-ε model

Since the dissipation rate of turbulent kinetic energy, ε appears naturally in the exact equation for turbulent kinetic energy, a two equation EVM with these two turbulent quantities would be a good choice in the formation of ν_t. The Low Reynolds Number (LRN) k-ε model used in this work is suggested by Abe-Kondoh-Nagano [1] commonly referred to as AKN model. The modeled k and ε equations read,

$$\frac{\partial k}{\partial t} + \overline{U_j}\frac{\partial k}{\partial x_j} = \frac{\partial}{\partial x_j}\left[\left(\nu + \frac{\nu_t}{\sigma_k}\right)\frac{\partial k}{\partial x_j}\right] + P_k - \varepsilon \tag{2.14}$$

$$\frac{\partial \varepsilon}{\partial t} + \overline{U_j}\frac{\partial \varepsilon}{\partial x_j} = \frac{\partial}{\partial x_j}\left[\left(\nu + \frac{\nu_t}{\sigma_\varepsilon}\right)\frac{\partial \varepsilon}{\partial x_j}\right] + C_{\varepsilon 1}\frac{\varepsilon}{k}P_k - C_{\varepsilon 2}f_2\frac{\varepsilon^2}{k} \tag{2.15}$$

where,

$$P_k = \left[\nu_t\left(\frac{\partial \overline{U_i}}{\partial x_j} + \frac{\partial \overline{U_j}}{\partial x_i}\right)\right]\frac{\partial \overline{U_i}}{\partial x_j} \tag{2.16}$$

$$\nu_t = C_\mu f_\mu \frac{k^2}{\varepsilon} \tag{2.17}$$

and,

$$f_\mu = \left[1 - \exp\left(-\frac{n^*}{14}\right)\right]^2\left[1 + \frac{5}{R_t^{3/4}}\exp\left\{-\left(\frac{R_t}{200}\right)^2\right\}\right]$$

$$f_2 = \left[1 - \exp\left(-\frac{n^*}{3.1}\right)\right]^2\left[1 - 0.3\,\exp\left\{-\left(\frac{R_t}{6.5}\right)^2\right\}\right]$$

$$n^* = \frac{\varepsilon^{1/4} n}{\nu^{3/4}}$$

where 'n' is the wall-normal distance between the node and the wall. The model constants are given by,

$C_\mu = 0.09$	$C_{\varepsilon 1} = 1.5$	$C_{\varepsilon 2} = 1.9$	$\sigma_k = 1.4$	$\sigma_\varepsilon = 1.4$

The turbulent length scale is given by,

$$l = \frac{k^{3/2}}{\varepsilon} \tag{2.18}$$

Time scale is obtained using velocity scale and the length scale,

$$\mathcal{T} = \frac{l}{\mathcal{V}} = \frac{l}{k^{1/2}} = \frac{k^{3/2}}{\varepsilon k^{1/2}} = \frac{k}{\varepsilon} \tag{2.19}$$

Wall Boundary Condition

On the wall,

$$\overline{U} = \overline{V} = k = 0 \tag{2.20}$$

$$\varepsilon_{wall} = 2\nu\frac{k_1}{n_1^2} \tag{2.21}$$

where n_1 is the wall normal distance for the near wall node.

2.3.2 Realizability and production (P_k) limiter

In this section we will discuss the changes made to original Abe-Kondoh-Nagano $k-\varepsilon$ model. In order to limit the growth of turbulent kinetic energy, we have used the following two different methods.

Realizability

The realizability constraint is expressed in terms of a limit on the turbulent time scale, $\mathcal{T}$. The following expression shows the time-scale constraint derived for $k-\varepsilon$ model (see [8] for derivation),

$$\mathcal{T} = \min\left(\frac{k}{\varepsilon}, \frac{0.6}{\sqrt{6}C_\mu f_\mu S}\right) \tag{2.22}$$

where, S is the strain rate tensor, S_{ij}. It should be noted that the time scale appears both in ν_t expression and ε equation.

Production (P_k) limiter

This is an explicit method of limiting the production of turbulent kinetic energy. The production term in the modelled k equation is modified as,

$$P_k = \min\left(2\nu_t S^2, a\,\varepsilon\right) \tag{2.23}$$

where, a = 2.5, was found to be the optimal value by Aldo [6].

2.3.3 Realizable $\overline{v^2}-f$ model

During the last few years the $\overline{v^2}-f$ turbulence model, originally suggested by Durbin [3], has become increasingly popular due to its ability to account for near-wall damping without use of damping functions. The $\overline{v^2}-f$ model has also shown to be superior to other RANS methods in many fluid flows where more complex flow features are present. The advantages of the model have attracted quite a few CFD researchers and several of them have suggested modifications to the original model. The

present $\overline{v^2} - f$ model investigated in this work is suggested by Kalitzin [4]. The modelled equations read,

$$\frac{\partial k}{\partial t} + \overline{U_j}\frac{\partial k}{\partial x_j} = \frac{\partial}{\partial x_j}\left[\left(\nu + \frac{\nu_t}{\sigma_k}\right)\frac{\partial k}{\partial x_j}\right] + P_k - \varepsilon \tag{2.24}$$

$$\frac{\partial \varepsilon}{\partial t} + \overline{U_j}\frac{\partial \varepsilon}{\partial x_j} = \frac{\partial}{\partial x_j}\left[\left(\nu + \frac{\nu_t}{\sigma_\varepsilon}\right)\frac{\partial \varepsilon}{\partial x_j}\right] + \frac{C_{\varepsilon 1}P_k - C_{\varepsilon 2}\varepsilon}{\mathcal{T}} \tag{2.25}$$

$$\frac{\partial \overline{v^2}}{\partial t} + \overline{U_j}\frac{\partial \overline{v^2}}{\partial x_j} = \frac{\partial}{\partial x_j}\left[\left(\nu + \frac{\nu_t}{\sigma_k}\right)\frac{\partial \overline{v^2}}{\partial x_j}\right] + kf - 6\overline{v^2}\frac{\varepsilon}{k} \tag{2.26}$$

$$L^2\frac{\partial^2 f}{\partial {x_j}^2} - f = \frac{C_1}{T}\left(\frac{\overline{v^2}}{k} - \frac{2}{3}\right) - C_2\frac{P_k}{k} - \frac{1}{T}\left(5\frac{\overline{v^2}}{k} - 0\right) \tag{2.27}$$

where,

$$P_k = 2\nu_t S^2 \;\; S^2 = S_{ij}S_{ij} \tag{2.28}$$

$$\nu_t = C_\mu \overline{v^2}\mathcal{T} \tag{2.29}$$

$$L = C_L \max\left(\frac{k^{3/2}}{\varepsilon}\;,\; C_\eta\frac{\nu^{3/4}}{\varepsilon^{1/4}}\right) \tag{2.30}$$

C_μ	$C_{\varepsilon 1}$	$C_{\varepsilon 2}$	C_1	C_2	σ_k	σ_ε	C_L	C_η
0.22	0.045	1.9	0.4	0.3	1.0	1.3	0.23	70

Wall boundary condition

On the wall,

$$\overline{U} = \overline{V} = k = f = \overline{v^2} = 0 \tag{2.31}$$

$$\varepsilon_{wall} = 2\nu\frac{k_1}{n_1^2} \tag{2.32}$$

Where n_1 is the wall normal distance for the near wall node.

Realizability

The realizability constraint used here is based on the $\overline{v^2} - f$ model by Lien and Kalitzin [5]. They use the same constraint on the turbulent time scale as was originally suggested by Durbin with the addition of a model constant, hereafter referred to as C_{lim} set to 0.6, leading to

$$\mathcal{T} = \min\left[\max\left(\frac{k}{\varepsilon}\ ,\ 6\sqrt{\frac{\nu}{\varepsilon}}\right)\ ,\ \frac{C_{lim}k}{\sqrt{6}C_{\mu}\overline{v^2}S}\right] \tag{2.33}$$

Chapter 3

Numerical method and the flow domain

3.1 The solver CALC-BFC

Computations were carried out using a finite volume computer code, CALC-BFC (Boundary Fitted Coordinates) by Davidson and Farhanieh [2]. CALC-BFC is written for two or three dimensional, steady/unsteady, turbulent/laminar recirculating flows. The code uses collocated variable arrangement and Cartesian velocity components on a general non-orthogonal Boundary Fitted Coordinate system for prediction of mass, heat, and momentum transfer. Various differencing schemes are available to approximate the convective fluxes: Central, Hybrid central upwind differencing, the QUICK scheme or the van-Leer scheme. The TDMA (Tri-Diagonal Matrix Algorithm) is then adapted to solve the descritised equations.

3.2 The flow domain

The flow domain as shown in Figure 3.1 has a *trailing-edge* plate of thickness, h = 1 and length, $L = 5$. The height of the $inlet$ on either side of the *trailing-edge* plate is 8 units. The geometry is as specified by Yao et al [11] and they have further studied domain dependency and concluded that the 2D computational box as in Figure 3.1 is large enough to study the flow phenomena.

3.3 The grid

A Low Reynolds Number mesh is generated with the near wall node located at $y^+ < 1$, and about 8-10 nodes within $y^+ < 10$. As suggested by Sohankar [7] in order to make sure that vortex-shedding behind the trailing edge was independent of grid spacing, the following condition

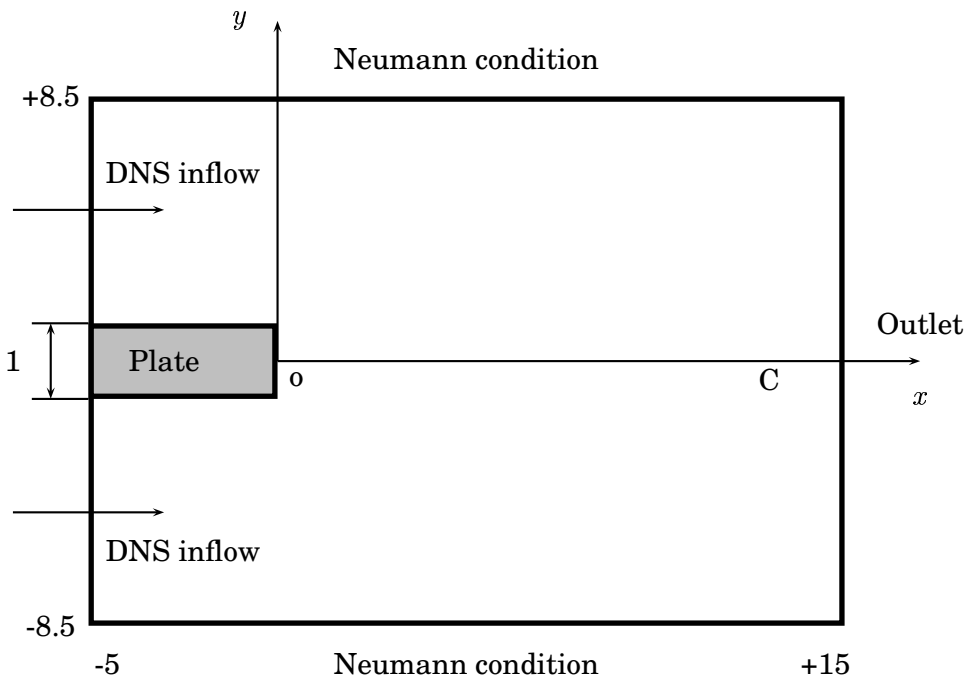

Figure 3.1: Flow domain

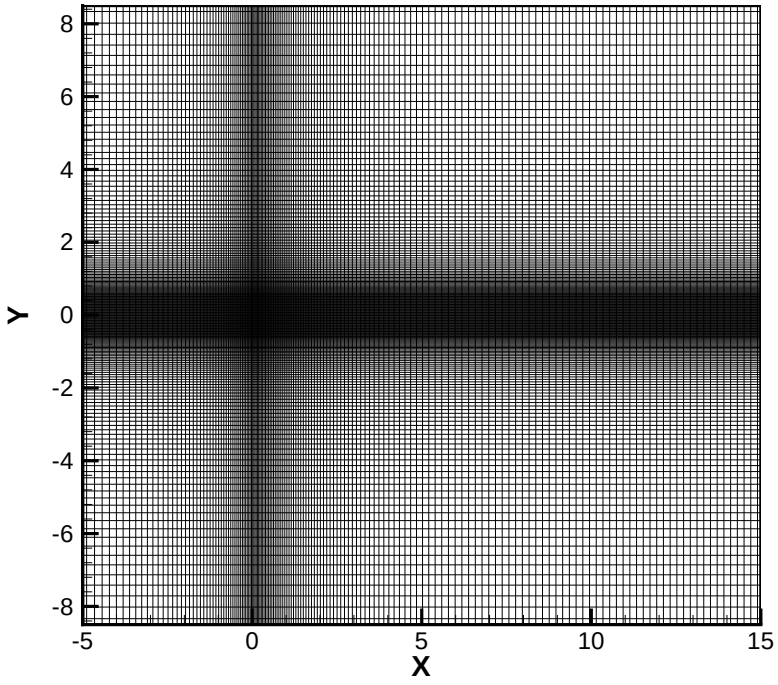

Figure 3.2: A fine mesh of 31 200 grid points

was satisfied while generating the grid:

$$\Delta x < 0.2\ h$$
$$\Delta y < 0.2\ h$$

where Δx and Δy are the streamwise and cross-streamwise grid spacing respectively. As an example a fine mesh of $31\,200$ grid points is shown in Figure 3.2.

3.4 Numerical schemes

Time marching was carried out using Crank-Nikolson scheme. For the convection and diffusion terms second-order central difference scheme was applied. van-Leer scheme was also tried in order to investigate the influence of numerical schemes on unsteady vortex shedding. For more information on schemes please refer Versteegh and Malalasekera [9].

3.5 Boundary conditions

Inlet

Turbulence mean properties from the DNS provided by Yao et al [12] is used at the inlet; the inflow boundary-layer thickness is 6.42 times the *trailing-edge* thickness, close to typical turbine blade flow applications.

Other

The wall boundary conditions were already discussed in section 2.3.1. For all other boundaries including the outlet Neumann boundary condition was used.

3.6 The TDMA solver

The TDMA (Tri-Diagonal Matrix Algorithm) is actually a formula for recursive use of solving matrix equations using Gauss-elimination. CALC-BFC employs a segregated TDMA solver which is discussed below for a 2D case with variable ϕ. The finite volume discretisation gives a penta-diagonal system in 2D. The 2D discretised equation is given by,

$$a_P\phi_P = a_E\phi_E + a_W\phi_W + a_N\phi_N + a_S\phi_S + S_U \tag{3.1}$$

Rewriting the above equation in the form,

$$a_i\phi_i = b_i\phi_{i+1} + c_i\phi_{i-1} + d_i \tag{3.2}$$

where,

$$a_i = a_P, b_i = a_E, c_i = a_W, d_i = a_N\phi_N + a_S\phi_S + S_U \tag{3.3}$$

Now we want to write 3.2 on the form,

$$\phi_i = P_i \phi_{i+1} + Q_i \tag{3.4}$$

In order to derive 3.4 we write 3.2 on matrix form as,

$$\begin{bmatrix} a_2 & -b_2 & 0 & \cdots & & \\ -c_3 & a_3 & -b_3 & o & \cdots & \\ 0 & -c_4 & a_4 & -b_4 & 0 & \cdots \\ \vdots & \vdots & \vdots & \vdots & \vdots & \vdots \end{bmatrix} \begin{bmatrix} \phi_2 \\ \phi_3 \\ \phi_4 \\ \vdots \end{bmatrix} = \begin{bmatrix} d_2 + c_2\phi_1 \\ d_3 \\ d_4 \\ \vdots \end{bmatrix}$$

Divide first row by a_2,

$$\begin{bmatrix} 1 & -P_2 & 0 & \cdots & & \\ -c_3 & a_3 & -b_3 & o & \cdots & \\ 0 & -c_4 & a_4 & -b_4 & 0 & \cdots \\ \vdots & \vdots & \vdots & \vdots & \vdots & \vdots \end{bmatrix} \begin{bmatrix} \phi_2 \\ \phi_3 \\ \phi_4 \\ \vdots \end{bmatrix} = \begin{bmatrix} Q_2 \\ d_3 \\ d_4 \\ \vdots \end{bmatrix}$$

where,

$$P_2 = \frac{b_2}{a_2}, Q_2 = \frac{d_2 + c_2\phi_1}{a_2} \tag{3.5}$$

To eliminate c in the second row, multiply first row by c_3, add it to second row and finally divide the entire second row by $a_3 - c_3 P_2$ to obtain,

$$\begin{bmatrix} 1 & -P_2 & 0 & \cdots & & \\ 0 & 1 & -P_3 & o & \cdots & \\ 0 & -c_4 & a_4 & -b_4 & 0 & \cdots \\ \vdots & \vdots & \vdots & \vdots & \vdots & \vdots \end{bmatrix} \begin{bmatrix} \phi_2 \\ \phi_3 \\ \phi_4 \\ \vdots \end{bmatrix} = \begin{bmatrix} Q_2 \\ Q_3 \\ d_4 \\ \vdots \end{bmatrix}$$

where,

$$P_3 = \frac{b_3}{a_3 - c_3 P_2}, Q_3 = \frac{d_3 + c_3 Q_2}{a_3 - c_3 P_2} \tag{3.6}$$

Now we see that 3.6 becomes a recursive equation for P_i and Q_i of the form,

$$P_i = \frac{b_i}{a_i - c_i P_{i-1}}, Q_i = \frac{d_i + c_i Q_{i-1}}{a_i - c_i P_{i-1}} \tag{3.7}$$

3.4 is solved from $i = 3$ to $i_{max} - 1$.

Chapter 4

Implementation of blockage

The *trailing-edge* plate forms the structural component in the flow domain. For the computation we have used single-block version of CALC-BFC. Therefore in order to implement this solid material in the numerical domain we have made some changes to the code. This chapter explains the *implementation* and *validation* of the blockage.

4.1 Implementation

The dependent variables ($\Phi's$) are set to zero

The first step is to set all the dependent variables ($\Phi's$) i.e., u, v, pp, k, ε to zero for each node inside the blocked domain. This is implemented as follows:
Set,

$$\begin{aligned} \Phi(i,j,k) &= 0.0 \\ SU(i,j,k) &= 0.0 \\ SP(i,j,k) &= -10^{20} \end{aligned}$$

Thereby in the descritised equation the value of Φ at each blocked node yields,

$$\Phi_P = \frac{\sum a_{NX}\Phi_{NX} + SU}{\sum a_{NX} - SP} \simeq 0 \tag{4.1}$$

where, a_{NX} are the co-efficients a_N, a_S, a_W and a_E.

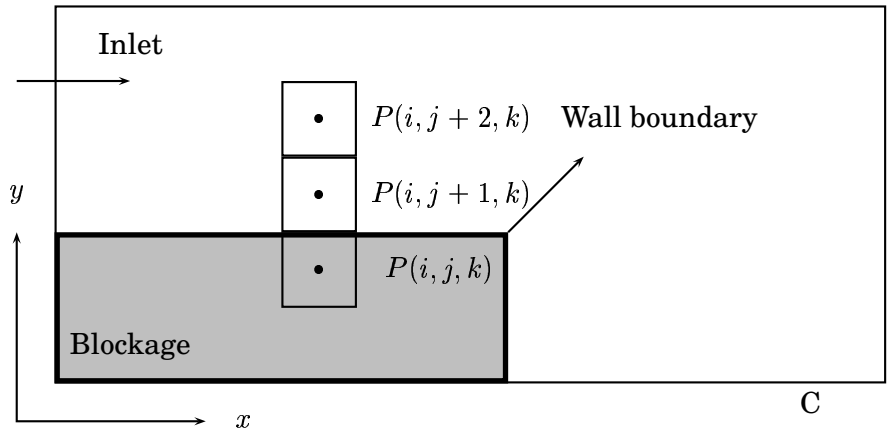

Figure 4.1:

Extrapolate pressure

In collocated grid arrangement we employ Rhie-Chow interpolation to eliminate pressure oscillations. Since Rhie-Chow uses nodes in the blockage, pressure is extrapolated for all the cells along the blocked surface in the appropriate direction . Here is an example for the cell along the north boundary face of the blockage.

By extrapolation the pressure at node (i, j, k) in Figure 4.1 is fixed as follows,

$$P(i, j, k) = 2 \times P(i, j+1, k) - P(i, j+2, k) \tag{4.2}$$

Similarly for cells along the east face of the blockage is extrapolated in x direction.

Set the convections to zero

Set the convections through all the faces i,e., north,south,east and west faces of each cell inside the blocked domain to zero.

Modify the weight functions

As we see in Figure 4.2 the wall boundary of the *trailing-edge* plate coincides with the grid lines. Do notice that there are no nodes on the wall! Therefore to fix the wall-boundary condition we need to fix the ϕ_s and ϕ_w equal to zero i.e., in Figure 4.2,

$$\text{Wall boundary condition} \Longrightarrow \Phi_s(j+1) = 0; \Phi_s(j-1) = 0; \Phi_w(i) = 0$$

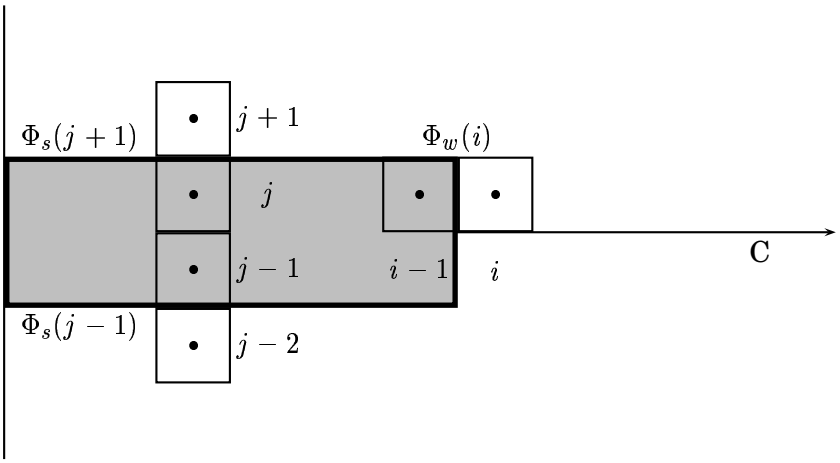

Figure 4.2:

The easiest way to implement this is by modifying the weight functions f_x and f_y. Let's illustrate how it is done.

We know that,

$$\Phi_s(j+1) = f_y(j)\Phi(j+1) + (1 - f_y(j))\Phi(j) \tag{4.3}$$
$$\Phi_s(j-1) = f_y(j-2)\Phi(j-1) + (1 - f_y(j-2))\Phi(j-2) \tag{4.4}$$
$$\Phi_w(i) = f_x(i-1)\Phi(i) + (1 - f_x(i-1))\Phi(i-1) \tag{4.5}$$

Now all we have to do is fix,

$$f_y(j) = 0$$
$$f_y(j-2) = 1$$
$$f_x(i-1) = 0$$

Since all the dependent variables inside the blockage are already set to zero, $4.3, 4.4, 4.5$ becomes,

$$\Phi_s(j+1) = \Phi(j) \equiv 0 \tag{4.6}$$
$$\Phi_s(j-1) = \Phi(j-1) \equiv 0 \tag{4.7}$$
$$\Phi_w(i) = \Phi(i-1) \equiv 0 \tag{4.8}$$

Also one should note that by modifying the weight functions even the gradients $\partial\phi/\partial y$, $\partial\phi/\partial x$ and so on are computed correctly.

Force $\nu_t = \nu$ inside the blockage

Set the eddy-viscosity, ν_t equal to kinematic viscosity, ν for each node inside the blocked domain.

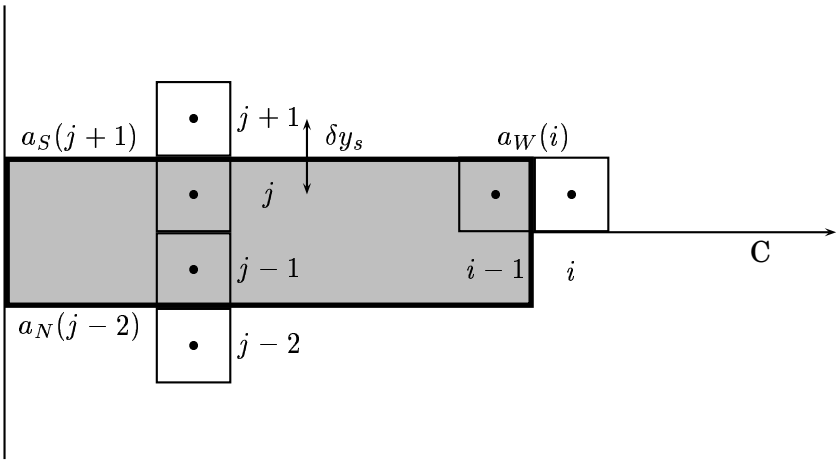

Figure 4.3:

Modify the coefficients a_N, a_S and a_W

The coefficients a_N, a_S and a_W for the near wall nodes have to be redefined each time after it is computed such that the new value is twice that of computed value. We will see below why and how it is modified. The coefficient $a_S(j+1)$ (see Figure 4.3) is computed as follows,

$$a_S(j+1) = \frac{\Gamma_s Area_s}{\delta y_s} \tag{4.9}$$

Where Γ is the diffusion co-efficient. We can see from the Figure that the distance between the near wall node $(j+1)$ and the wall is $\delta y_s/2$. Therefore we should evaluate the coefficient only over this distance. which implies,

$$a_S(j+1) = \frac{\Gamma_s Area_s}{\delta y_s/2} \tag{4.10}$$

Therefore fix,

$$a_S(j+1) = 2\, a_S(j+1) \tag{4.11}$$

$$\text{similarly, } a_N(j-2) = 2\, a_N(j-2) \tag{4.12}$$

$$a_W(i) = 2\, a_W(i) \tag{4.13}$$

4.2 Validation

The implimented code is tested for the precision and functionality. Steady channel flow simulations were computed on different geometries and turbulence models.

In Figure 4.4 (a), if we block half the domain then the resulting flow domain is exactly same as that in Figure 4.4 (b). With the same inlet

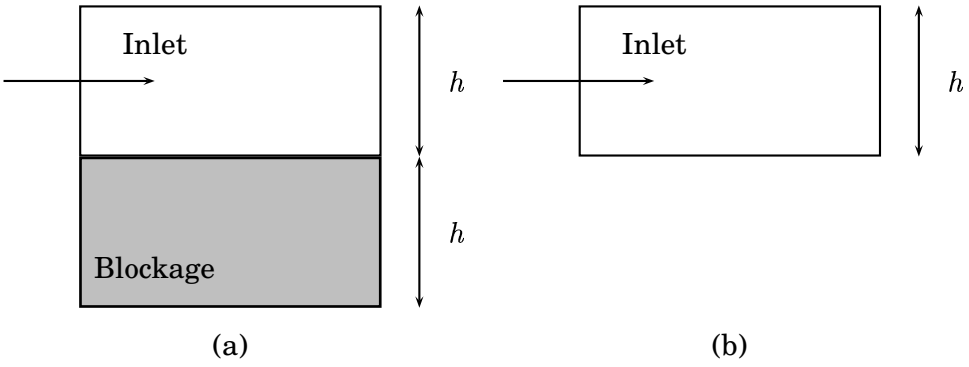

Figure 4.4: Test 1

boundary condition channel flow is simulated in both the geometries and compared against each other. Two turbulence models, a LRN $k-\omega$ model suggested by Wilcox [10] and a LRN $k-\varepsilon$ model (AKN) were tested on this geometry.

Figure 4.5: Test 2

Channel flow is also simulated in the above geometry (see Figure 4.5) with two inlets above and below the blockage. Here also LRN $k-\varepsilon$ model (AKN) was used.

Chapter 5

Results and discussion

5.1 Grid refinement study

The unsteady RANS calculations were carried out with several different grid resolutions. The Table below illustrates the parameters for the three cases tested. The near-wall grid resolution is characterized by the number of points across the trailing-edge end (N_{TE}), the number of points in the sublayer region $y^+ < 10$ (N_{Sub}) and the distance of the first point from the solid wall in wall units (y_1^+). The streamwise grid resolution, $\Delta x^+ (= u^* \, \Delta x/\nu)$, is calculated in wall units for the boundary-layer. The streamwise grid size, Δx_{bl} and Δx_{wake}, in both boundary-layer and wake regions are also shown in the table.

Case	Nodes	N_{TE}	N_{Sub}	y_1^+	Δx_{bl}^+	Δx_{bl}	Δx_{wake}
1	15300	50	8	0.47	$4.6 - 26.2$	$0.07 - 0.4$	$0.05 - 0.5$
2	31200	50	9	0.51	$2.2 - 13.2$	$0.04 - 0.2$	$0.03 - 0.2$
3	43000	50	11	0.40	$2.1 - 13.0$	$0.03 - 0.2$	$0.03 - 0.19$

All the three test cases were computed using $k - \varepsilon$ model (AKN) with realizability constraint. Figure 5.1 shows the streamwise mean velocity U variations along the centerline of the trailing-edge. The mean velocity changes from coarse grid (case 1) to finer grid (case 2) and collapses with the finest grid (cases 3), indicating that the simulation with a grid of 156×200 (case 2) gives a good resolution of the flow. The time step, Δt, was also refined in order to confirm that the solution was independent of time step resolution. $\Delta t = 0.047$ was found appropriate for all the computations.

5.2 Vortex shedding

Figure 5.2(a) and 5.2(b) shows instantaneous pressure ($\overline{P}$) and transverse ($\overline{V}$) velocity contours from $k - \varepsilon$ model (AKN) with realizability

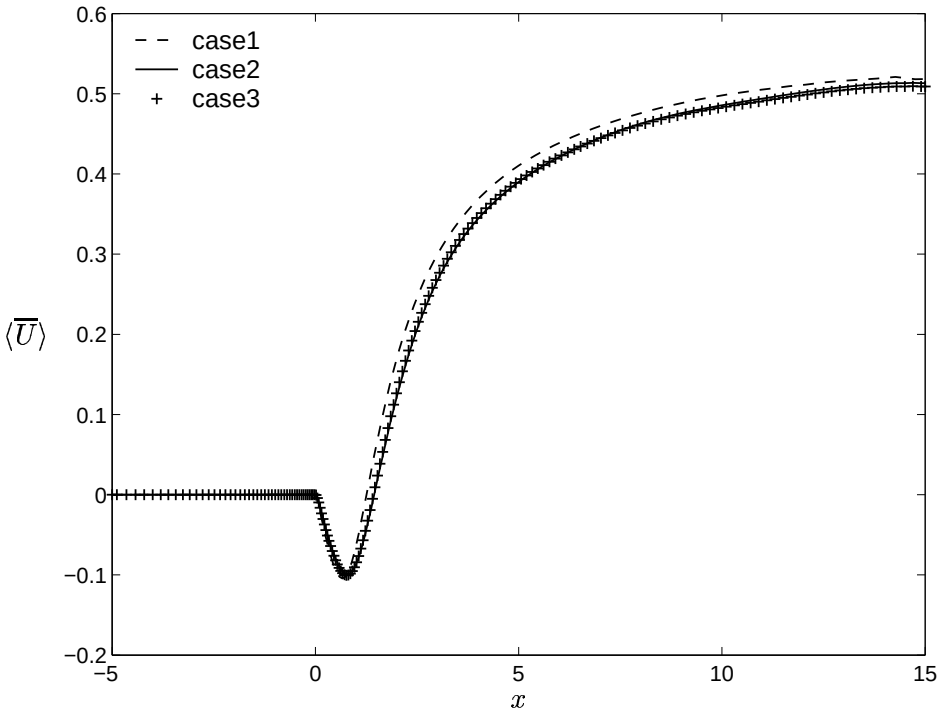

Figure 5.1: Grid refinement study

constraint, indicating clearly the oscillating shedding behaviour. To investigate the flow unsteadiness associated with vortex shedding in detail, we determine the shedding frequency using lift and pressure drag coefficients defined as,

$$C_L \simeq \frac{1}{\frac{1}{2}\,\rho\,U_e^2 A}\int_A (\overline{P}_l - \overline{P}_u)\,ds \;\simeq\; \frac{1}{\frac{1}{2}\,\rho\,U_e^2 L}\int_{-5}^{0} (\overline{P}_l - \overline{P}_u)\,dx \quad (5.1)$$

$$C_D \simeq \frac{1}{\frac{1}{2}\,\rho\,U_e^2 A}\int_A \overline{P}\,ds \;\simeq\; \frac{1}{\frac{1}{2}\,\rho\,U_e^2 h}\int_{-0.5}^{+0.5} \overline{P}\,dx \quad (5.2)$$

where ρ and U_e are the freestream density and velocity respectively. $(\overline{P}_l - \overline{P}_u)$ indicates the difference of pressure between the lower and upper plates. For the lift coefficient, the integral is performed over the plate horizontal length of $L = 5$. This truncation of the semi-infinite domain to 5 is not considered serious for interpreting the shedding behaviour. For the pressure drag coefficient, the integral is performed over the plate height of $h = 1$.

As an example, Figure 5.2(c) and 5.2(d) shows the time history of the C_L and C_D computed from $k - \varepsilon$ model (AKN). It should be noted that

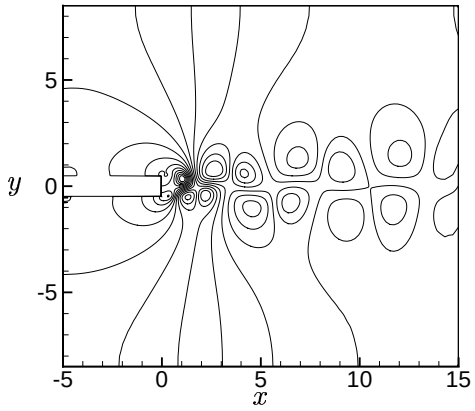

(a) $\overline{P}$, with realizability constraint

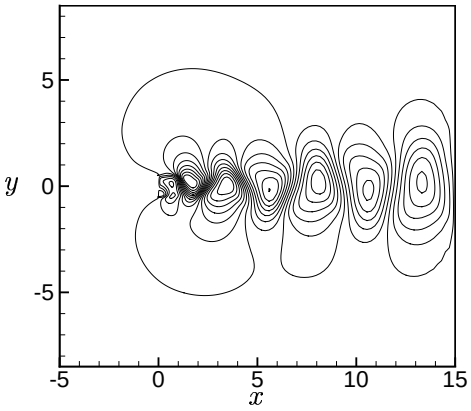

(b) $\overline{V}$, with realizability constraint

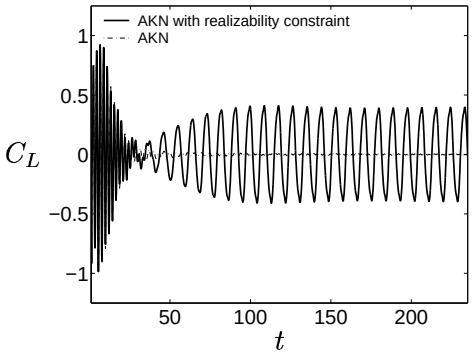

(c) C_L

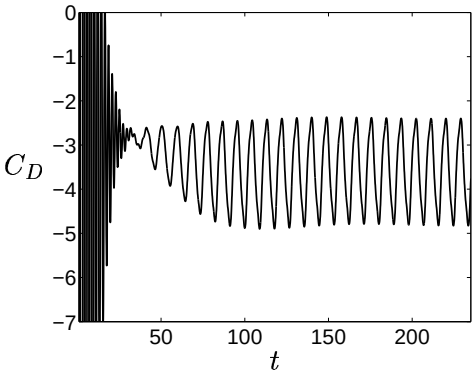

(d) C_D, with realizability constraint

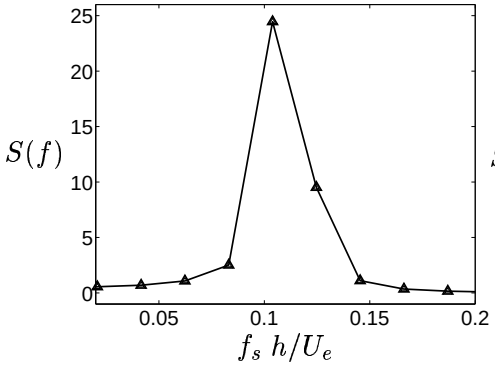

(e) St, with realizability constraint

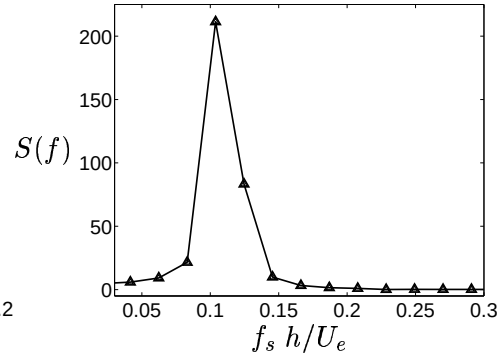

(f) St, with realizability constraint

Figure 5.2: Vortex shedding behaviour by $k-\varepsilon$ model (AKN): (a,b) instantaneous pressure ($\overline{P}$) and $\overline{V}$-velocity contours ; (c,d) time history of C_L and C_D; (e,f) power spectrum of C_L and C_D respectively, showing peaks at a Strouhal number St(=$f_s h/U_e$) = 0.104

(see Figure 5.2(c)) $k-\varepsilon$ model (AKN) fails to capture unsteady vortex shedding. Only when used with realizability constraint or P_k limiter, the model starts exhibiting unsteady behaviour. A precise estimation of shedding frequency, f_s, was obtained from the spectral analysis of C_L and C_D. The power spectrum of C_L and C_D (see Figure 5.2(e) and 5.2(f)) gives the main shedding frequency, f_s. The Strouhal number, St = $f_s h/U_e$, was found to be very close to the DNS value. The Table below illustrates the vortex shedding parameters predicted by different turbulence models.

Model	St	$C_{L'}$	$C_{D'}$
$k-\varepsilon$ model (AKN) with realizability constraint	0.104	0.282	0.832
$k-\varepsilon$ model (AKN) with P_k limiter	0.104	0.157	0.507
$\overline{v^2}-f$ model with realizability constraint	0.104	0.296	0.959
DNS by Yao et al [11]	0.115	N/A	N/A

5.3 Velocity profiles and streamlines

Figure 5.3(a) shows the mean streamwise velocity, $\langle\overline{U}\rangle$ contours. Figure 5.3(b), 5.3(c) and 5.3(d) shows the recirculation bubble forming downstream the trailing-edge. The bubble predicted by URANS (all three cases) has a similar shape and length close to that of DNS [11]. To investigate the bubble formation, streamlines were plotted at different instances in time in one period (T=8.883 seconds). Figure 5.4 illustrates the separation bubble positions at different instances in time (t).

To study the performance of models, mean streamwise velocity, $\langle\overline{U}\rangle$, from all the three cases were plotted along the centreline (see Figure 5.5). Both $\overline{v^2}-f$ model with realizability constraint and $k-\varepsilon$ model (AKN) with realizability constraint give similar results downstream but vary in the near wake. Figure 5.6(a) shows the streamwise mean velocity profiles in the wall normal direction at seven streamwise locations (first two in the boundary layer, next two in the near wake and the rest downstream).

5.4 Resolved and modelled quantities

5.4.1 Resolved and modelled turbulent kinetic energy

Figure 5.7(a) and 5.7(b) shows the time-averaged resolved and modelled turbulent kinetic energy contours as predicted by $k-\varepsilon$ model (AKN) with realizability constraint. As seen in Figure 5.7(a), a strange contour appears at the outlet, indicating the existance of oscillating shedding behaviour at the outlet. On such occasions *convective outlet boundary condition* is more realistic than the one we used (Neumann boundary

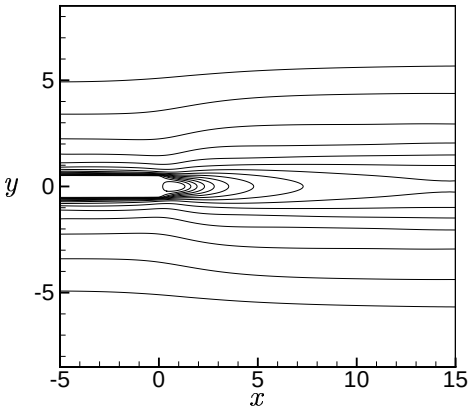

(a) $k - \varepsilon$ with realizability constraint

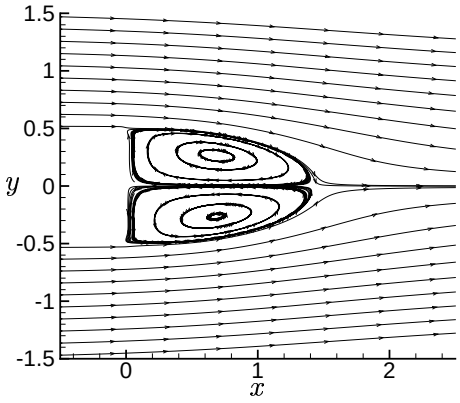

(b) $k - \varepsilon$ with realizability constraint (close-up view showing separation bubble)

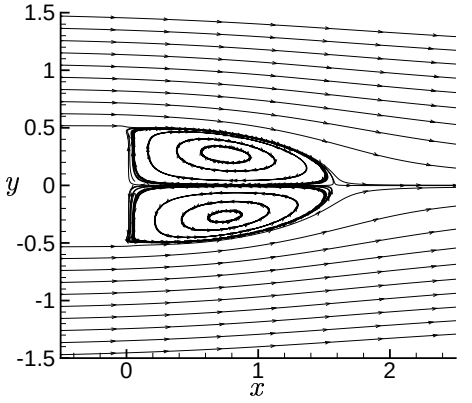

(c) $k - \varepsilon$ with P_k limiter (close-up view)

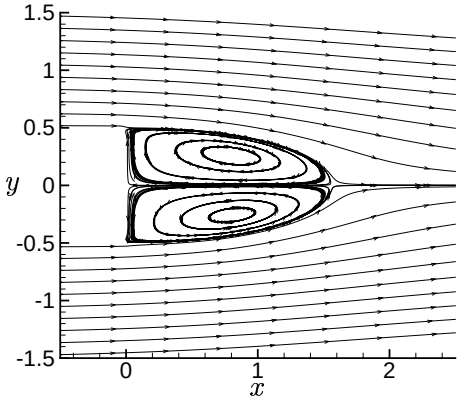

(d) $\overline{v^2} - f$ with realizability constraint (close-up view)

Figure 5.3: Steamwise mean velocity contour, $\langle \overline{U} \rangle$

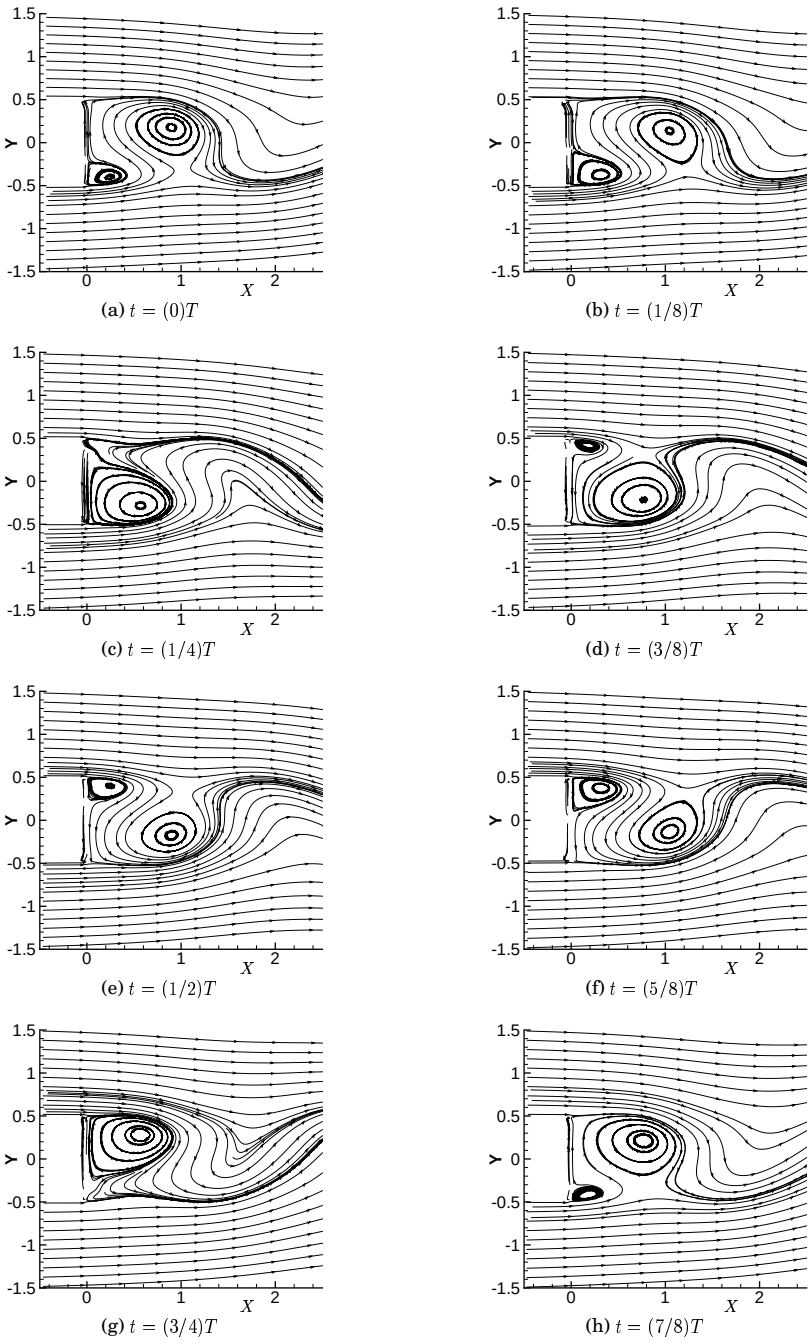

Figure 5.4: Instantaneous streamlines showing separation bubbles at different instances in one period, T (=8.883 seconds). The streamlines are as predicted by $k - \varepsilon$ model (AKN) with realizability constraint

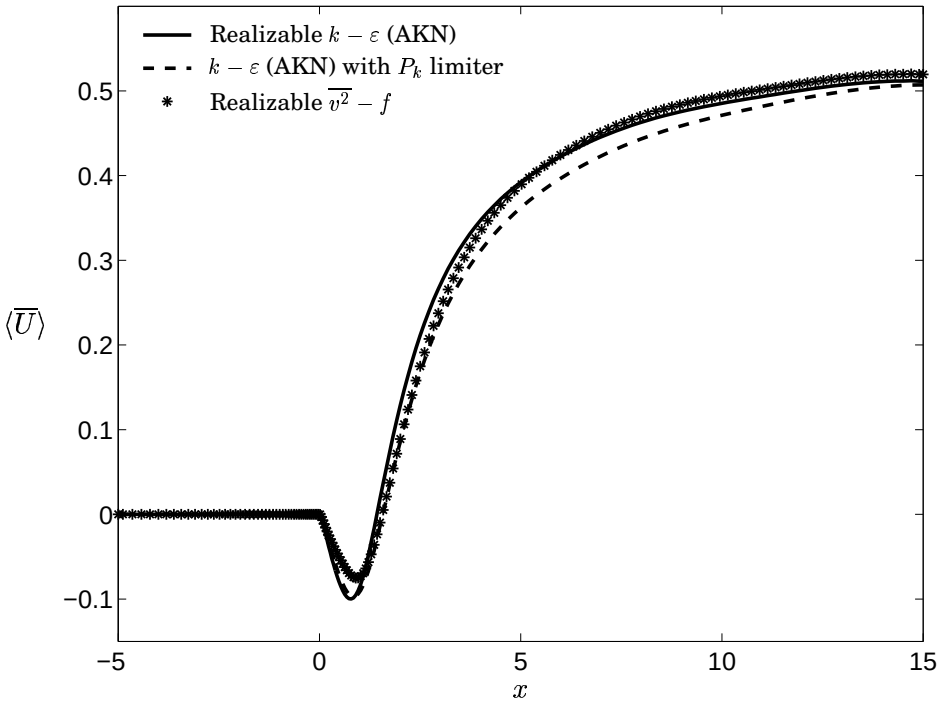

Figure 5.5: Steamwise mean velocity along the centreline

condition). It should be noted that if the vortex shedding dies within the computational box then the use of Neumann boundary condition is appropriate.

To study the extent at which modelled ($k_{modelled}$) and resolved ($k_{resolved}$) kinetic energies affect the total turbulence kinetic energy (k_{total}), Figure 5.7(c), 5.7(d) and 5.7(e) are plotted for all the three models. In the realizable models, both $k_{modelled}$ and $k_{resolved}$ contributes towards the k_{total}, while with the P_k limiter, modelled turbulent kinetic energy dominates. Figure 5.7(f) illustrates the modelled kinetic energy variations in the wall normal direction at seven streamwise locations.

5.4.2 Dissipation

Figure 5.8 shows the modelled dissipation (ε) contour predicted by $k-\varepsilon$ model (AKN) with realizability constraint. To investigate the model performance, energy dissipation is plotted along the centreline for all the three models (see Figure 5.9). Figure 5.10 illustrates ε profiles in the wall normal direction at seven streamwise locations. When compared with the DNS [11] value, only $\overline{v^2}-f$ model gives better results in the near wake. It was also found that all the three models show good agreement with DNS in the boundary layer and far downstream.

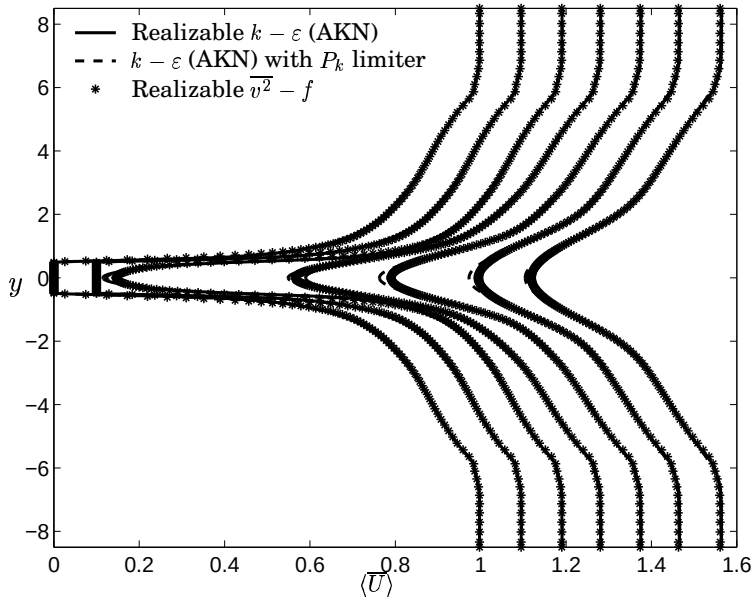

(a) Global view

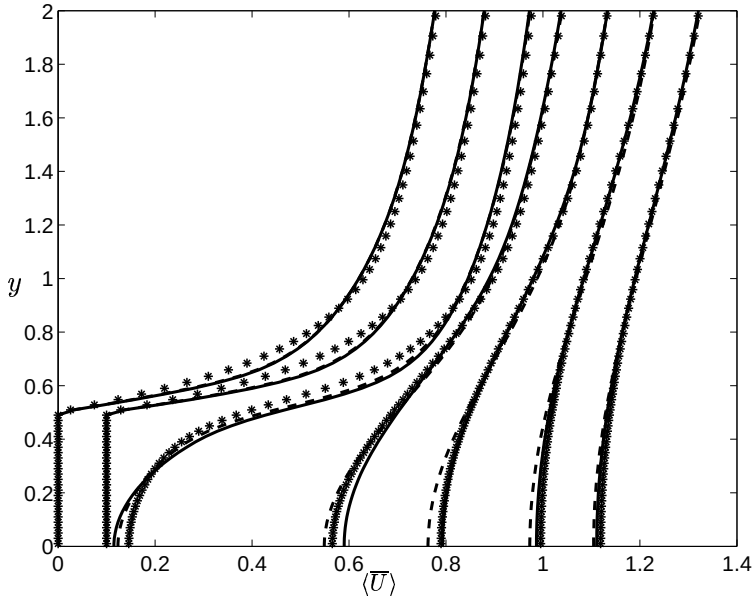

(b) Close-up view

Figure 5.6: Streamwise mean velocity profiles in the wall normal direction at seven streamwise locations (x = -3, -1, 0.5, 3, 5, 10, 14). Note that, for clarity, profiles at successive x-locations have been shifted to the right by 0.1

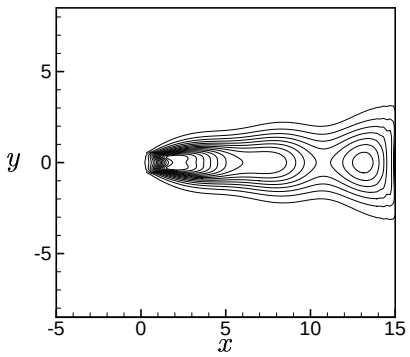

(a) $k_{resolved}$

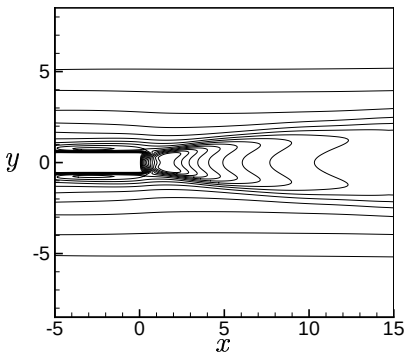

(b) $k_{modelled}$

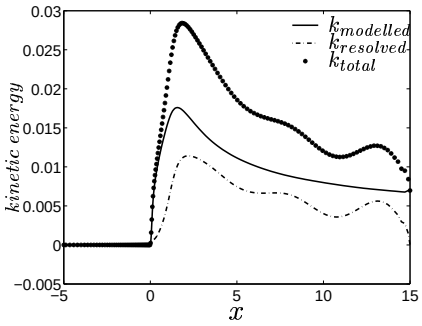

(c) Realizable $k-\varepsilon$ (AKN)

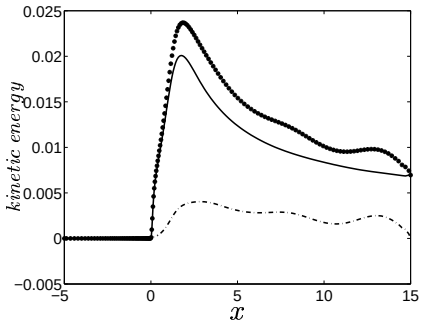

(d) $k-\varepsilon$ (AKN) with P_k limiter

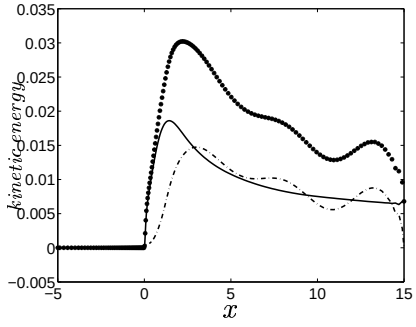

(e) Realizable $\overline{v^2}-f$

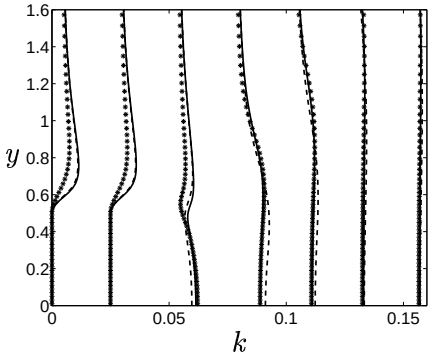

(f) $k_{modelled}$

Figure 5.7: (a,b) resolved and modelled kinetic energy contours from $k-\varepsilon$ model (AKN) with realizability constraint; (c,d,e) comparison of modelled, resolved and total kinetic energy; (f) modelled kinetic energy profiles in the wall normal direction at seven streamwise locations (x = -3, -1, 0.5, 3, 5, 10, 14). Profiles at successive x-locations have been shifted to the right by 0.025. The legend is as per Figure 5.6(a).

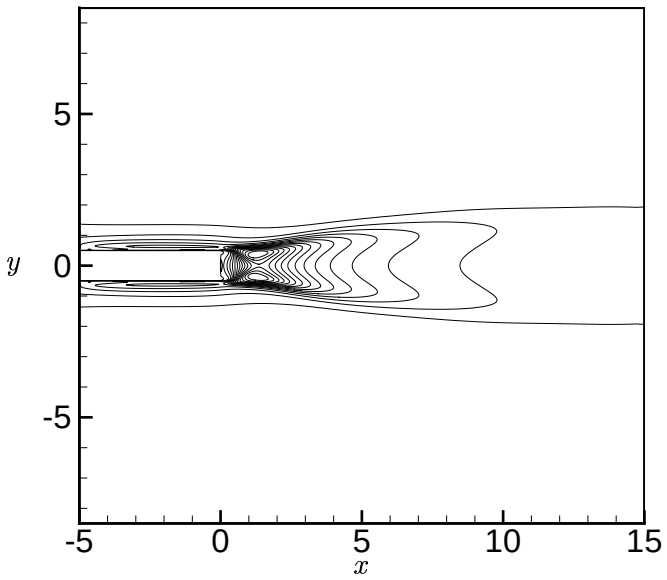

Figure 5.8: Energy dissipation contour from $k - \varepsilon$ model (AKN) with realizability constraint

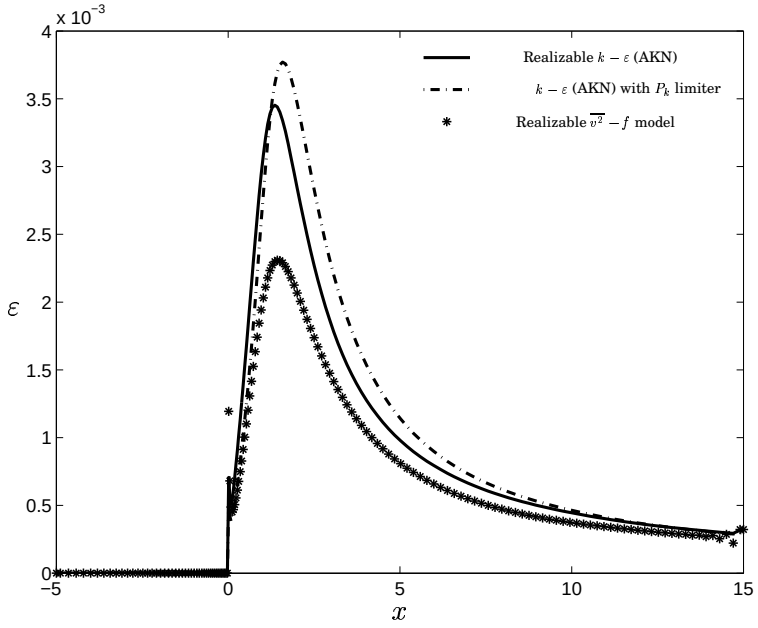

Figure 5.9: Energy dissipation profiles along the centreline for three different cases

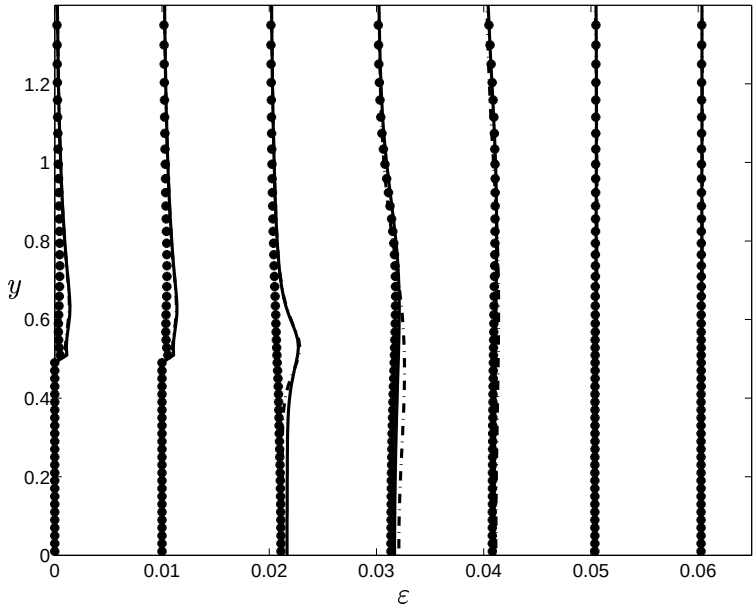

Figure 5.10: Energy dissipation profiles in the wall normal direction at seven streamwise locations (x = -3, -1, 0.5, 3, 5, 10, 14). Profiles at successive x-locations have been shifted to the right by 0.01. The legend is as per Figure 5.9.

5.4.3 Resolved and modelled stresses

Figure 5.11(a) and 5.11(b) show the resolved normal stresses, $\overline{u^2}$ and $\overline{v^2}$ as predicted by $k-\varepsilon$ (AKN) model with realizability constraint. $\overline{u^2}$ and $\overline{v^2}$ profiles are also plotted in the wall normal direction at seven streamwise locations (see Figure 5.11(c), 5.11(d)). The variation of $\overline{uv}_{resolved}$ and $\overline{uv}_{modelled}$ in the wall normal direction at seven streamwise locations is also shown in Figure 5.11(e) and 5.11(f)

5.5 Influence of discretizing scheme

In the previous sections we have investigated various turbulence models and their subsequent effect on unsteady vortex shedding. A similar investigation was carried out to study the influence of discretizing schemes on unsteady vortex shedding. In this section we have used van-Leer scheme instead of central difference scheme for convection-diffusion terms. Figure 5.12(a) and 5.12(b) shows the time history of C_L and power spectrum of C_L respectively. It should be noted that both the schemes have predicted the same Strouhal number ($St = 0.104$).

As we know that van-Leer scheme is bounded and dissipative in nature, we expected the van-Leer scheme to produce lower RMS lift and drag

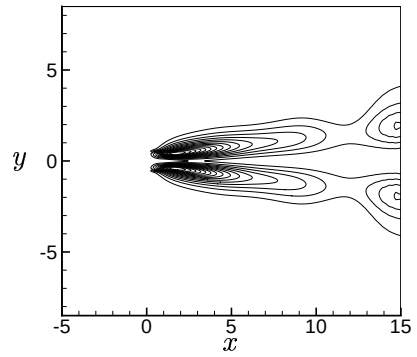

(a) $\overline{u^2}_{resolved}$

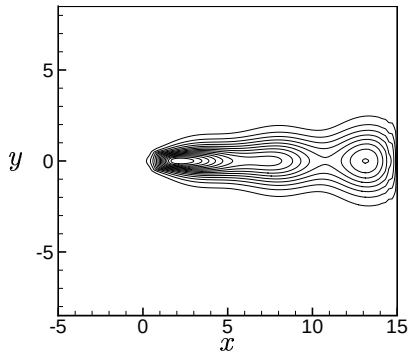

(b) $\overline{v^2}_{resolved}$

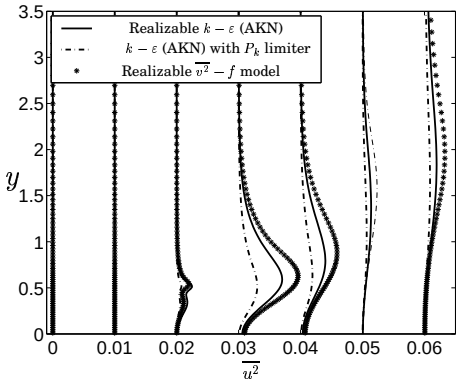

(c) $\overline{u^2}_{resolved}$

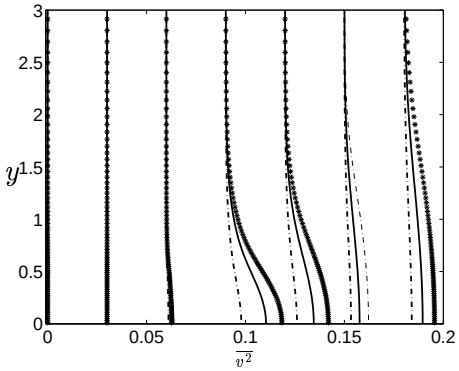

(d) $\overline{v^2}_{resolved}$

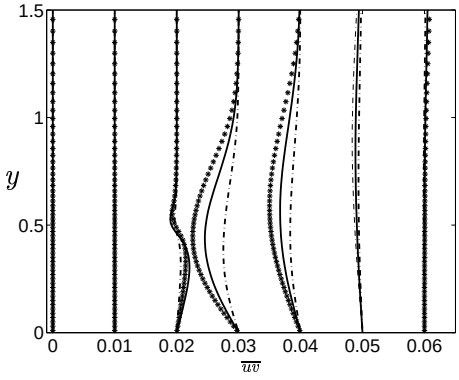

(e) $\overline{uv}_{resolved}$

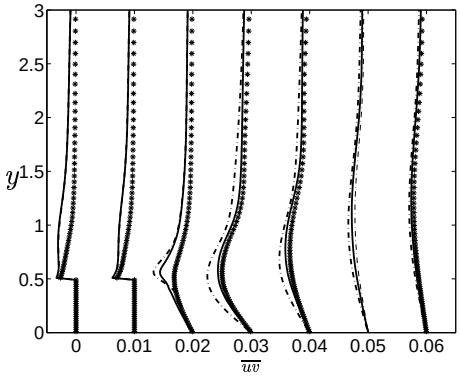

(f) $\overline{uv}_{modelled}$

Figure 5.11: (a,b) resolved normal stress contours from $k-\varepsilon$ model (AKN) with realizability constraint; (c,d,e,f) profiles in the wall normal direction at seven streamwise locations (x = -3, -1, 0.5, 3, 5, 10, 14). Profiles at successive x-locations have been shifted to the right by 0.01.

coefficients ($C_{L'}$ and $C_{D'}$) and consequently producing lower resolved kinetic energy compared to central difference scheme. The Table below illustrates the vortex shedding parameters predicted by both the schemes with the same turbulence model ($k-\varepsilon$ model (AKN) with realizability constraint).

Discretizing Scheme	St	$C_{L'}$	$C_{D'}$
Central Difference	0.104	0.282	0.832
van-Leer	0.104	0.089	0.865

It should be noted from the table that van-Leer scheme predicts a higher value of $C_{D'}$ compared to central difference scheme. Also if we look into the Figure 5.12(c) and 5.12(d), we can see that van-Leer scheme produces higher resolved kinetic energy compared to central difference scheme; the reason for which is not clear and has to be investigated.

Figure 5.12(e) and 5.12(f) illustrates the mean stream velocity and energy dissipation variations along the centreline for both the schemes.

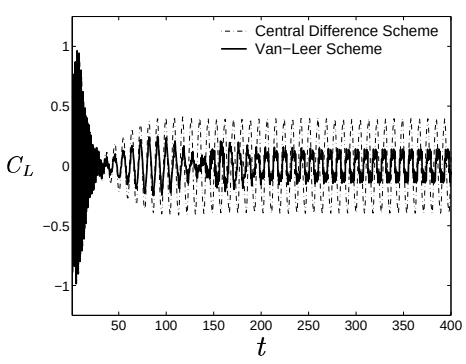

(a) Time history of C_L

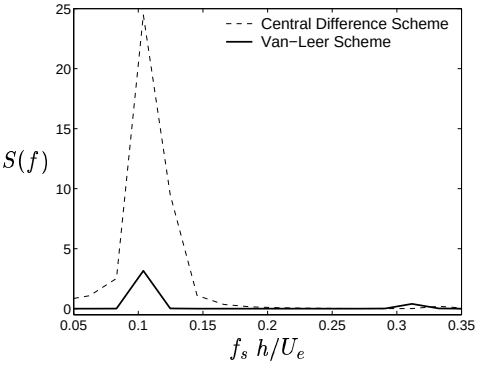

(b) Strouhal number (St)

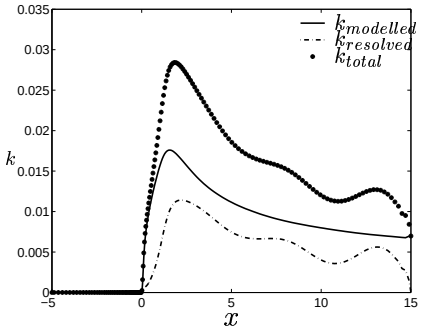

(c) Central difference scheme

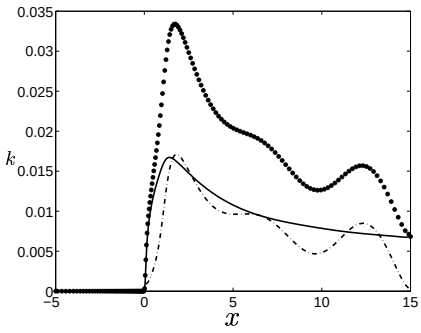

(d) van-Leer scheme

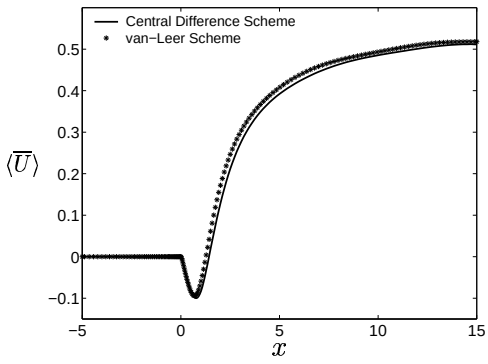

(e) $\langle\overline{U}\rangle$ along the centreline

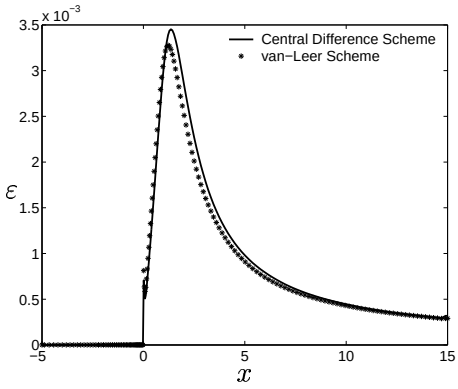

(f) ε along the centreline

Figure 5.12: Comparison of central difference scheme and van-Leer scheme by using $k-\varepsilon$ model (AKN) with realizability constraint: (b) power spectrum of C_L, showing peaks at a Strouhal number St(=$f_s h/U_e$) = 0.104; (c,d) comparison of modelled, resolved and total kinetic energy; (e,f) streamwise mean velocity and energy dissipation along the centreline.

Chapter 6

Conclusions

The LRN $k-\varepsilon$ model by AKN [1] fails to capture unsteady vortex shedding.

Flow unsteadyness was produced by both LRN $k-\varepsilon$ model (with realizability constraint or P_k limiter) and Realizable $\overline{v^2}-f$ model.

Strouhal number (St) was found very close to the DNS value, irrespective of the turbulence model and discretizing scheme employed.

Separation bubble size from URANS was found close to the DNS bubble size, indicating good prediction of reverse flow.

Streamwise mean velocity and total kinetic energy values come closer to DNS.

The unsteady turbulence is found to be of comparable importance to the modelled turbulence in the near wake, especially when the models use realizability constraint.

The overall performance of LRN $k-\varepsilon$ model (with realizability constraint) and realizable $\overline{v^2}-f$ model is better compared to $k-\varepsilon$ model (with P_k limiter).

It was found that van-Leer scheme (bounded and dissipative in nature) produces higher resolved kinetic energy compared to central difference scheme; the reason for which is not clear and has to be investigated.

Chapter 7

Future Work

Studying the effect of *convective outlet boundary condition* instead of Neumann boundary condition at the outlet.

Increasing the domain size streamwise, to investigate if the solution is sensitive to the location of the outlet.

Performing a unsteady 3D computation to study the influence of 3D effects.

Bibliography

[1] K. Abe, T. Kondoh, and Y. Nagano. A new turbulence model for predicting fluid flow and heat transfer in separating and reattaching flows - 1. Flow field calculations. *Int. J. Heat Mass Transfer*, 37:139–151, 1994.

[2] L. Davidson and B. Farhanieh. CALC-BFC: A finite-volume code employing collocated variable arrangement and cartesian velocity components for computation of fluid flow and heat transfer in complex three-dimensional geometries. Rept. 95/11, Dept. of Thermo and Fluid Dynamics, Chalmers University of Technology, Gothenburg, 1995.

[3] P.A. Durbin. Near-wall turbulence closure modeling without damping functions. *Theoretical and Computational Fluid Dynamics*, 3:1–13, 1991.

[4] G. Kalitzin. Application of the $\overline{v^2} - f$ model to aerospace configurations. Center for Turbulence Research Annual Research Briefs, 1999.

[5] F. Lien and G. Kalitzin. Computations of transonic flow with the $\overline{v^2} - f$ turbulence model. *Int. J. Heat Fluid Flow*, 22:53–61, 2001.

[6] A.G.B. Moran. Prediction of the axisymmetric impinging jet with different $k - \varepsilon$ turbulence models. Diploma work, Dept. of Thermo and Fluid Dynamics, Chalmers University of Technology, Göteborg, Sweden, 2004.

[7] A. Sohankar. *Numerical Study of Laminar,Transitional and Turbulent Flow Past Rectangular Cylinders*. PhD thesis, Dept. of Thermo and Fluid Dynamics, Chalmers University of Technology, Göteborg, Sweden, 1998.

[8] A. Sveningsson. Analysis of the performance of different $\overline{v^2} - f$ turbulence models in a stator vane passage flow. Thesis for licentiate of engineering, Dept. of Thermo and Fluid Dynamics, Chalmers University of Technology, Göteborg, Sweden, 2003.

[9] H.K. Versteegh and W. Malalasekera. *An Introduction to Computational Fluid Dynamics - The Finite Volume Method*. Longman Scientific & Technical, Harlow, England, 1995.

[10] D.C. Wilcox. Reassessment of the scale-determining equation. *AIAA Journal*, 26:1299–1310, 1988.

[11] Y.F. Yao, A.M. Savill, N.D. Sandham, and W.N. Dawes. Simulation and modelling of turbulent trailing-edge flow. *Flow, Turbulence and Combustion*, 68:313–333, 2002.

[12] Y.F. Yao, T.G. Thomas, N.D. Sandham, and J.J.R. Willi ams. Direct numerical simulation of turbulent flow over a recta ngular trailing edge. *Theoretical and Computational Fluid Dynamics*, 14:337–358, 2001.